Centrum voor Wiskunde en Informatica

REPORT*RAPPORT*

MAS

Modelling, Analysis and Simulation

Modelling, Analysis and Simulation

Efficient computation of steady, 3D water-wave patterns, application to hovercraft-type flows

M.R. Lewis, B. Koren

REPORT MAS-R0232 DECEMBER 31, 2002

CWI is the National Research Institute for Mathematics and Computer Science. It is sponsored by the Netherlands Organization for Scientific Research (NWO).
CWI is a founding member of ERCIM, the European Research Consortium for Informatics and Mathematics.

CWI's research has a theme-oriented structure and is grouped into four clusters. Listed below are the names of the clusters and in parentheses their acronyms.

Probability, Networks and Algorithms (PNA)

Software Engineering (SEN)

Modelling, Analysis and Simulation (MAS)

Information Systems (INS)

P.O. Box 94079, 1090 GB Amsterdam (NL)
Kruislaan 413, 1098 SJ Amsterdam (NL)
Telephone +31 20 592 9333
Telefax +31 20 592 4199

ISSN 1386-3703

Efficient Computation of Steady, 3D Water-Wave Patterns, Application to Hovercraft-Type Flows

Mervyn Lewis and Barry Koren
CWI
P.O. Box 94079, 1090 GB Amsterdam, The Netherlands

ABSTRACT
Numerical methods for the computation of stationary free surfaces is the subject of much current research in computational engineering. The present report is directed towards free surfaces in maritime engineering. Of interest here are the long steady waves generated by hovercraft and ships, the gravity waves. In the present report an existing 2D iterative method for the computation of stationary gravity-wave solutions is extended to 3D, numerically investigated, and improved. The method employs the so-called quasi free-surface boundary condition. As test cases we consider gravity-wave patterns due to hovercraft-type pressure perturbations imposed at the free surface of a steady, uniform horizontal flow. The effects are studied of the distance of the imposed pressure distribution to the far-field boundary, the magnitude of the imposed pressure perturbation, the mesh widths, as well as the presence of a no-slip boundary intersecting the free surface. In all experiments, our focus is on the convergence behavior of the free-surface iteration process.
2000 Mathematics Subject Classification: 35R35,76D05,76D33.
Keywords and Phrases: incompressible Navier-Stokes equations, free-surface methods for partial differential equations, water waves.
Note: This work was supported by the Dutch Technology Foundation STW, and was carried out under CWI-project MAS 2.1 "Computational Fluid Dynamics". The authors want to thank dr. Hoyte Raven of MARIN for his useful comments.

1. Introduction

Examples of free-surface problems in science and engineering are vast. The applications we are aiming at are the water-wave patterns generated by a hovercraft or ship hull moving with steady, rectilinear velocity.

The inherent difficulty of computing free-surface flows is the interdependence of the free-surface location and the unknowns of the flow problem. Numerical techniques available for the computation of free-surface flows can be divided into two categories: the *fixed*-grid (Eulerian) and the *moving*-grid (Lagrangian) methods. See the introduction of [1] for a general overview of these methods. In the case of a smooth free surface without overturning waves, i.e., when the free surface can be represented by a height function, surface-fitting methods are unsurpassed in accuracy. Because our primary focus is on the computation of non-overturning gravity waves, this method is adopted here.

The main topic of this work is the investigation of the convergence behavior for 3D problems, of a new non-monolithic (i.e., an alternating or partitioned) free-surface iteration method, proposed and worked out in [2] for 2D flows. In [2], the so-called quasi free-surface boundary condition is derived. In the present paper, this boundary condition is extended to 3D and the free-surface iteration method is applied to a test case involving stationary gravity waves induced by a pressure perturbation imposed at the free surface of a 3D water flow. Varying the amplitude of the perturbation alters the nonlinearity of the resulting wave system. Each step of the free-surface iteration method involves the solution of a stationary Navier-Stokes boundary-value problem. In an improved version of the free-surface algorithm (to be presented in Section 5), the Navier-Stokes equations are not fully solved per free-surface iteration, but only corrected through a single relaxation sweep. The numerical results are compared with a solution of the potential-flow method from [3].

The contents of this report is the following. In Section 2, the governing equations are introduced. Section 3 describes the computational method, in particular the stationary Navier-Stokes boundary-value problem which is solved in each free-surface iteration step. In Section 4, various numerical results are presented for the free-surface algorithm. In Section 5, an improvement is made to the algorithm and corresponding numerical results are presented. Section 6 concludes the paper.

2. Governing equations and free-surface boundary conditions

In this section an outline is given of the mathematical model which describes viscous free-surface flows. The first subsection lists the equations which describe the fluid flow, the next subsection treats the free-surface boundary conditions and the last the so-called quasi free-surface boundary condition.

2.1 Flow equations

Let $\Omega(\mathbf{x}) \subset \mathbb{R}^3$ be the physical domain which is occupied by the fluid and let us split the domain boundary as $\partial\Omega = \Gamma_{\rm FS} \cup \Gamma_0$, where $\Gamma_{\rm FS}$ denotes the free surface and Γ_0 the remaining (fixed) part of $\partial\Omega$. Positions in $\mathbb{R}^3$ are identified with respect to a Cartesian coordinate system $\mathbf{e}_\alpha$, $\alpha = \{x, y, z\}$. The state of the flow is characterized by the velocity field $\mathbf{u}(\mathbf{x}) : \Omega \to \mathbb{R}^3$ and the pressure $p(\mathbf{x}) : \Omega \to \mathbb{R}$. Incompressibility implies a solenoidal velocity field:

$$\nabla \cdot \mathbf{u}(\mathbf{x}) = 0, \quad \forall \mathbf{x} \in \Omega. \tag{2.1}$$

Conservation of momentum of the fluid is described by

$$\nabla \cdot (\mathbf{u}\mathbf{u}^T) + \nabla\varphi - \mathrm{Re}^{-1}\tilde{\Delta}\mathbf{u} = \mathbf{0}, \quad \forall \mathbf{x} \in \Omega, \tag{2.2}$$

where $\mathrm{Re} = U\ell/\nu$ is the Reynolds number, with U and ℓ a reference speed and length and with ν the kinematic viscosity. The unknown φ is the hydrodynamic pressure

$$\varphi(\mathbf{x}) := p(\mathbf{x}) + \mathrm{Fr}^{-2} z, \tag{2.3}$$

which contains the second similarity parameter in viscous free-surface flows, the Froude number, $\mathrm{Fr} \equiv U/\sqrt{g\ell}$, with g the acceleration of gravity. It is assumed that diffusion in main flow direction, say the x-direction, can be safely neglected. As a result the viscous term reduces to $\tilde{\Delta} = \partial_y^2 + \partial_z^2$, which in turn reduces the number of boundary conditions to be imposed at the x-outlet boundary.

2.2 Free-surface boundary conditions

The free-surface boundary conditions follow from the general interface conditions and the assumptions that both density and viscosity of one of the adjacent fluids vanish at the interface and that the interface is impermeable. In many applications of interest, especially in those which admit steady solutions, the free surface can be expressed as a single-valued height function η: $\Gamma_{\rm FS} = \{(\mathbf{x}) : z = \eta(x, y)\}$. Impermeability leads to the steady form of the kinematic condition

$$\mathbf{u} \cdot \nabla\eta(x, y) = \mathbf{u} \cdot \mathbf{e}_z. \tag{2.4}$$

This formulation imposes smoothness restrictions on the shape of the free surface. Vanishing interfacial stresses result in three dynamic conditions, namely

$$p(\mathbf{x}) - 2\mathrm{Re}^{-1}\frac{\partial \mathbf{u}_n}{\partial \mathbf{n}} = p_{\rm FS}(\mathbf{x}), \tag{2.5}$$

in the direction normal to the free surface, with $p_{\rm FS}(\mathbf{x})$ the specified pressure perturbation along the free surface, and

$$\mathbf{t}^{(\alpha)} \cdot \tau(\mathbf{u}) \cdot \mathbf{n} = 0, \quad \alpha = 1, 2 \tag{2.6}$$

tangential to the free surface, where $\tau(\mathbf{u})$ is the viscous stress tensor for an incompressible fluid. Here $(\mathbf{n}, \mathbf{t}^{(\alpha)}), \alpha = 1, 2$ are the unit normal vector and the orthonormal tangential vectors, respectively. For the practical application envisaged here, the viscous contribution to the normal dynamic condition may be neglected, resulting in an inhomogeneous Dirichlet condition for the pressure $p(\mathbf{x})$. It has been assumed that surface tension effects can be safely ignored.

2.3 Quasi free-surface boundary condition

In free-surface flows, an interdependence exists of the state variables $(\mathbf{u}(\mathbf{x}), p(\mathbf{x}))$ and their spatial domain, through both the kinematic and dynamic conditions. In general, the free-surface flow problem is stated by equations (2.1), (2.2) subject to (2.4)–(2.6) on $\Gamma_{\rm FS}$, together with additional boundary conditions on Γ_0. Many concurrent free-surface iteration methods apply a formulation in which they

first solve (2.1), (2.2), in time-dependent form, subject to the dynamic conditions at an approximate location of the free surface. In the following step, they adjust the free surface using the kinematic condition in time-dependent form. Results obtained with these methods can be found in, e.g., [5, 6] for the fully time-dependent approach and in, e.g., [7, 8] for pseudo-time integration and quasi-steady methods.

In this report we apply a different free-surface iteration method based on the use of the quasi free-surface boundary condition, which states

$$\mathrm{Fr}^2\mathbf{u}(\mathbf{x})\cdot\nabla\varphi(\mathbf{x})-\mathbf{u}(\mathbf{x})\cdot\mathbf{e}_z=\mathrm{Fr}^2\mathbf{u}\cdot\nabla p_{\mathrm{FS}},\quad\forall\mathbf{x}\in\Gamma_{\mathrm{FS}}. \tag{2.7}$$

The derivation and application in 2D of this boundary condition can be found in [2]. Use of this special free-surface condition has the advantage that it does not decouple the kinematic and dynamic free-surface conditions. In fact, it is the combination of these kinematic and dynamic conditions which yields the wave-like solutions.

3. Computational method

It has been shown that the usual time integration method to solve for steady state is computationally inefficient. This is due to the fact that the attenuation of gravity waves behaves like $\mathcal{O}(t^{(1-d)/2})$ in $\mathbb{R}^d$, see [2]. In Section 3.1 we outline our efficient iterative solution method for gravity-subjected free-surface flows. It requires the solution of a sequence of steady-state Navier-Stokes subproblems. A description of the latter is given in Section 3.2.

3.1 Free-surface iteration method

Denoting (2.1) and (2.2) as $\mathcal{C}(\mathbf{u}(\mathbf{x}),\varphi(\mathbf{x}))=0$, and the boundary conditions to be imposed at Γ_0 as $\mathcal{B}(\mathbf{u}(\mathbf{x}),\varphi(\mathbf{x}))=0$, the solution of the free-surface flow problem can be found by iterating the following two steps:

I. For a given boundary Γ_{FS}, solve $(\mathbf{u}(\mathbf{x}),\varphi(\mathbf{x}))^T$ from

$$\begin{aligned}&\mathcal{C}(\mathbf{u}(\mathbf{x}),\varphi(\mathbf{x}))=0,\quad\forall\mathbf{x}\in\Omega,\\&\mathcal{B}(\mathbf{u}(\mathbf{x}),\varphi(\mathbf{x}))=0,\quad\forall\mathbf{x}\in\Gamma_0,\end{aligned}$$

$$\left.\begin{aligned}&\mathbf{t}^{(\alpha)}\cdot\tau(\mathbf{u})\cdot\mathbf{n}=0,\quad\alpha=1,2\\&\mathrm{Fr}^2\mathbf{u}\cdot\nabla\varphi-\mathbf{u}\cdot\mathbf{e}_z=\mathrm{Fr}^2\mathbf{u}\cdot\nabla p_{\mathrm{FS}}\end{aligned}\right\},\quad\forall\mathbf{x}\in\Gamma_{\mathrm{FS}}.$$

If $\|p-p_{\mathrm{FS}}\|$ still exceeds a suitably chosen small tolerance (note that at convergence $p=p_{\mathrm{FS}}$), then do step II, else stop.

II. Use the solution $(\mathbf{u}(\mathbf{x}),\varphi(\mathbf{x}))^T$ of I to obtain a new approximation of Γ_{FS} according to

$$\{(x,y,z:=\mathrm{Fr}^2(\varphi(\mathbf{x})-p_{\mathrm{FS}}(\mathbf{x})):\forall\mathbf{x}\in\Gamma_{\mathrm{FS}}\}, \tag{3.1}$$

next return to step I.

3.2 Discrete Navier-Stokes boundary value problem

The free-surface iteration method of the previous section requires the solution of the reduced Navier-Stokes boundary-value problem mentioned in step I. The discretization of this boundary-value problem is outlined first.

3.2.1 Discrete flow equations Let Ω_h be the orthogonal and equidistant partitioning of $\bar{\Omega}(\mathbf{x})$, with $\mathbf{x}=(i\Delta x,j\Delta y,k\Delta z)$. On Ω_h we denote a grid function $f(i\Delta x,j\Delta y,k\Delta z)$ by $f_{i,j,k}$. At all grid points, both in the interior and at the boundaries, the derivatives are replaced by finite differences as specified below. As mentioned, x is associated with the main-flow direction. In the continuity and momentum equations all first-order velocity derivatives in the main-flow direction are discretized using an $\mathcal{O}(h^2)$ upwind-difference scheme with fixed bias. The remaining first-order velocity derivatives in the continuity equation and momentum equations are discretized using an $\mathcal{O}(h^3)$ upwind-biased difference scheme. The pressure term is discretized using an $\mathcal{O}(h^3)$ downwind-difference scheme again with a

fixed bias. The opposite biasing of the velocity divergence and the pressure gradient ensures discrete ellipticity, herewith avoiding 'odd-even decoupling' of the solution [9]. The second-order velocity derivatives are discretized with standard, second-order accurate central differences. In formula, the discrete continuity equation reads

$$\begin{aligned}
&\frac{3u_{i,j,k} - 4u_{i-1,j,k} + u_{i-2,j,k}}{2\Delta x} + \\
&\frac{2v_{i,j+1,k} + 3v_{i,j,k} - 6v_{i,j-1,k} + v_{i,j-2,k}}{6\Delta y} + \\
&\frac{2w_{i,j,k+1} + 3w_{i,j,k} - 6w_{i,j,k-1} + w_{i,j,k-2}}{6\Delta z} = 0,
\end{aligned} \tag{3.2}$$

and the discrete momentum equations, for positive $u_{i,j,k}$, $v_{i,j,k}$ and $w_{i,j,k}$:

$$\begin{aligned}
&u_{i,j,k}\frac{3u_{i,j,k} - 4u_{i-1,j,k} + u_{i-2,j,k}}{2\Delta x} + \\
&v_{i,j,k}\frac{2u_{i,j+1,k} + 3u_{i,j,k} - 6u_{i,j-1,k} + u_{i,j-2,k}}{6\Delta y} + \\
&w_{i,j,k}\frac{2u_{i,j,k+1} + 3u_{i,j,k} - 6u_{i,j,k-1} + u_{i,j,k-2}}{6\Delta z} + \\
&\frac{-\varphi_{i+2,j,k} + 6\varphi_{i+1,j,k} - 3\varphi_{i,j,k} - 2\varphi_{i-1,j,k}}{6\Delta x} + \\
&\frac{-1}{\mathrm{Re}}\left(\frac{u_{i,j+1,k} - 2u_{i,j,k} + u_{i,j-1,k}}{\Delta y^2} + \frac{u_{i,j,k+1} - 2u_{i,j,k} + u_{i,j,k-1}}{\Delta z^2}\right) = 0,
\end{aligned} \tag{3.3a}$$

$$\begin{aligned}
&u_{i,j,k}\frac{3v_{i,j,k} - 4v_{i-1,j,k} + v_{i-2,j,k}}{2\Delta x} + \\
&v_{i,j,k}\frac{2v_{i,j+1,k} + 3v_{i,j,k} - 6v_{i,j-1,k} + v_{i,j-2,k}}{6\Delta y} + \\
&w_{i,j,k}\frac{2v_{i,j,k+1} + 3v_{i,j,k} - 6v_{i,j,k-1} + v_{i,j,k-2}}{6\Delta z} + \\
&\frac{-\varphi_{i,j+2,k} + 6\varphi_{i,j+1,k} - 3\varphi_{i,j,k} - 2\varphi_{i,j-1,k}}{6\Delta y} + \\
&\frac{-1}{\mathrm{Re}}\left(\frac{v_{i,j+1,k} - 2v_{i,j,k} + v_{i,j-1,k}}{\Delta y^2} + \frac{v_{i,j,k+1} - 2v_{i,j,k} + v_{i,j,k-1}}{\Delta z^2}\right) = 0,
\end{aligned} \tag{3.3b}$$

$$\begin{aligned}
&u_{i,j,k}\frac{3w_{i,j,k} - 4w_{i-1,j,k} + w_{i-2,j,k}}{2\Delta x} + \\
&v_{i,j,k}\frac{2w_{i,j+1,k} + 3w_{i,j,k} - 6w_{i,j-1,k} + w_{i,j-2,k}}{6\Delta y} + \\
&w_{i,j,k}\frac{2w_{i,j,k+1} + 3w_{i,j,k} - 6w_{i,j,k-1} + w_{i,j,k-2}}{6\Delta z} + \\
&\frac{-\varphi_{i,j,k+2} + 6\varphi_{i,j,k+1} - 3\varphi_{i,j,k} - 2\varphi_{i,j,k-1}}{6\Delta z} + \\
&\frac{-1}{\mathrm{Re}}\left(\frac{w_{i,j+1,k} - 2w_{i,j,k} + w_{i,j-1,k}}{\Delta y^2} + \frac{w_{i,j,k+1} - 2w_{i,j,k} + w_{i,j,k-1}}{\Delta z^2}\right) = 0.
\end{aligned} \tag{3.3c}$$

3.2.2 Computational domain and boundary conditions In $\mathbb{R}^d$, a full Navier-Stokes problem requires d boundary conditions on all boundary planes. Due to the reduced viscous operator, only one boundary condition may be imposed at an outlet boundary perpendicular to the x-direction. All other boundary planes require d boundary conditions, hereafter referred to as *physical* boundary conditions.

Physical boundary conditions The computational domain is defined by $\bar{\Omega} = \{(x, y, z) : [x_{\mathrm{in}}, x_{\mathrm{out}}] \times [0, y_e] \times [z_b, \eta]\}$. At the boundaries of $\bar{\Omega}$ we impose the following conditions:

- **Inflow boundary** ($x = x_{\mathrm{in}}$). At this boundary three Dirichlet conditions are imposed in the form of specification of the velocity components, i.e.

$$\mathbf{u} = (U_\infty, 0, 0)^T. \tag{3.4}$$

- **Outflow boundary** ($x = x_{\text{out}}$). Here an inhomogeneous Neumann condition is imposed on the hydrodynamic pressure, viz.

$$\varphi_x = -uu_x. \tag{3.5}$$

Note the nonlinearity of this boundary condition.

- **External boundary** ($y = y_e$). Dirichlet conditions are imposed on the tangential velocity components u and w, and on the hydrodynamic pressure φ:

$$u = U_\infty, \quad w = 0, \quad \varphi = 0. \tag{3.6}$$

- **Internal boundary plane** ($y = 0$). The internal boundary is taken as a symmetry boundary. Homogeneous Neumann conditions are imposed on the tangential velocity components and a likewise homogeneous Dirichlet condition on the normal velocity component:

$$\frac{\partial u}{\partial y} = 0, \quad \frac{\partial w}{\partial y} = 0, \quad v = 0. \tag{3.7}$$

- **Bottom** ($z = z_b$). Also here, homogeneous Neumann conditions are imposed on the tangential velocity components, in this case u and v, and a homogeneous Dirichlet condition on the normal velocity component:

$$\frac{\partial u}{\partial z} = 0, \quad \frac{\partial v}{\partial z} = 0, \quad w = 0. \tag{3.8}$$

- **Free-surface boundary** ($z = \eta$). At the free surface the following set of boundary conditions is imposed. Vanishing of the tangential stress components at the free surface results in

$$\frac{\partial u}{\partial n} = 0, \quad \frac{\partial v}{\partial n} = 0, \tag{3.9}$$

with n the normal to the free surface. Further, a Gaussian pressure perturbation with the following form is prescribed:

$$p_{\text{FS}}(x, y) = Pe^{\alpha((x-x_c)^2+(y-y_c)^2)}, \quad P > 0, \quad \alpha < 0. \tag{3.10}$$

The location (x_c, y_c) of the maximum pressure, as well as the parameters P and α may be varied. Substituting (3.10) into the quasi free-surface boundary condition (2.7) leads to

$$\text{Fr}^2\mathbf{u} \cdot \nabla\varphi - \mathbf{u} \cdot \mathbf{e}_z = 2\text{Fr}^2\alpha p_{\text{FS}}(\mathbf{x})(\mathbf{u} \cdot \mathbf{r}), \quad \mathbf{r} = (x - x_c, y - y_c, 0)^T, \quad \forall \mathbf{x} \in \Gamma_{\text{FS}}. \tag{3.11}$$

Note the nonlinearity of the quasi free-surface boundary condition.

All Neumann boundary conditions are discretized using $\mathcal{O}(h^2)$ one-sided differences. The pressure gradient in the quasi free-surface boundary condition is discretized using an $\mathcal{O}(h^2)$ upwind-difference scheme.

Numerical boundary conditions Because the discretization stencils extend beyond the boundaries of the computational domain, for the numerical solution procedure, numerical boundary conditions are required (for filling the virtual grid points outside the computational domain). For this purpose, quadratic solution extrapolation from the interior is applied.

3.2.3 Solution method The discretized equations form a system of nonlinear algebraic equations, which is solved by Newton's method. The sparsity pattern of the resulting linear algebraic system favors an iterative solution method over a direct method. The linear system is solved by adopting a space-marching Gauss-Seidel algorithm in which the marching is performed in the main flow direction (the x-direction). This approach is natural in view of the strong parabolic nature of the flow equations.

The space-marching procedure yields a size reduction of the linear-algebra problem. The smaller linear systems are solved using a CILU(0) preconditioned Krylov-subspace method (GMRES). The search space for the Krylov method is limited to 20 vectors. The convergence criterion for the solution of the inner (Newton) iteration process is that the residuals of the bulk flow have all dropped below some very small threshold value. More details on the solution strategy of the system of algebraic equations are given in [9]. The method has been implemented in the computer code `PARNASSOS` [1].

[1] www.marin.nl/services/softwaredevelopment/cph_parnassos.html

4. Numerical results

In this section we present some numerical results obtained with the free-surface iteration method described in the previous section.

4.1 First results

As a first test case we consider the following parameter values for the Gaussian pressure perturbation (3.10): $P = 0.05$, $\alpha = -4$, Fr $= 0.6$ and $(x_c, y_c) = (0, 0)$. This is conform to computations done with the potential-flow method described in [4]. Re is set equal to 10^6. The current computation is performed on the basis mesh, Ω_h, which has 81, 31 and 31 nodes in the x-, y- and z-direction, respectively. Ω_h is constructed such that the Kelvin wedge, which bounds the spatial distribution of the wave energy, does not intersect the external boundary by taking $x_{\text{out}} = 6$ and $y_e = 3$. The wedge makes a semi-angle of 19.5° with the main flow direction. (See Section 3.10 in [10] for a derivation of this result.) Other boundary coordinates chosen are $x_{\text{in}} = -2$ and $z_b = -3$. For all computations, the initial estimate of the free surface is the plane $z = 0$.

As mentioned before, our focus is on the convergence behavior of the new free surface iteration method. We distinguish two iteration processes: an outer and an inner iteration process, the iteration processes II and I, respectively, as described in Section 3.1. The convergence of the outer iteration, the free-surface method, is measured through the pressure defect at the free surface. The convergence of the inner iteration, the Navier-Stokes method, is measured by computing $\|\mathbf{R}\|_\infty$, where $\mathbf{R}$ is the residual of the flow equations (3.2),(3.3). For the present test case, the convergence behavior of the inner iteration is shown in the left graph of Figure 1.

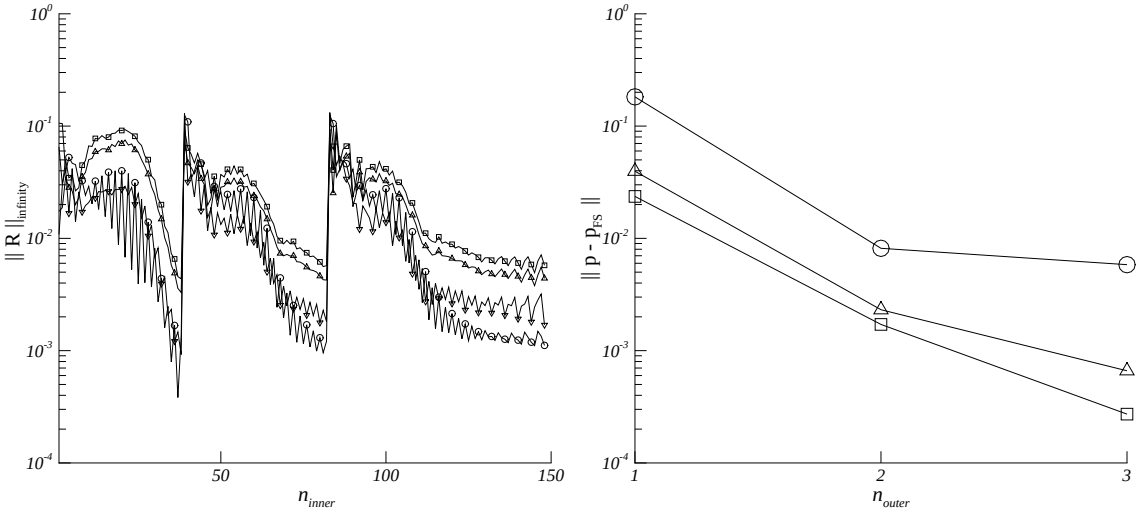

Figure 1: Convergence histories for the Gaussian pressure perturbation with $P = 0.05$, on Ω_h. *Left:* of the inner-iteration process, $\mathbf{R}$ is the residual of the continuity equation (Δ), the x-momentum equation ($\square$), the y-momentum equation (∇), and the z-momentum equation ($\bigcirc$), only every fourth marker is shown. *Right:* of the free-surface pressure defect; measured in L_1-norm ($\square$), L_2-norm (Δ), and L_∞-norm ($\bigcirc$).

The two large jumps in the residual (at about $n = 40$ and $n = 80$) are due to free-surface updates. After each free-surface update, the residuals are scaled, which explains the identical residual values after these updates. Figure 1 reveals that the inner-iteration process on the mesh obtained after the third free-surface update starts to oscillate with an increasing amplitude, preventing further decrease of the residuals. A closer inspection has shown that these residuals occur at a location near the outflow boundary, in the first grid plane underneath the free surface. This indicates a local incompatibility between the free-surface flow and the underlying bulk-flow solution. The proposed remedy will be addressed in the next section. The convergence of the free-surface iteration process is monitored through the pressure defect $\|p^n - p_{\text{FS}}\|$, measured in some usual norms. Here $p^n = \varphi^n - \text{Fr}^{-2} z^n$ is the hydrodynamic pressure minus the hydrostatic part. The decrease in the pressure defect is shown in the right graph of Figure 1. The free-surface iteration appears to converge very fast; the second and third free-surface updates are already negligibly small as compared to the first, as can be seen in the

left graph of Figure 2.

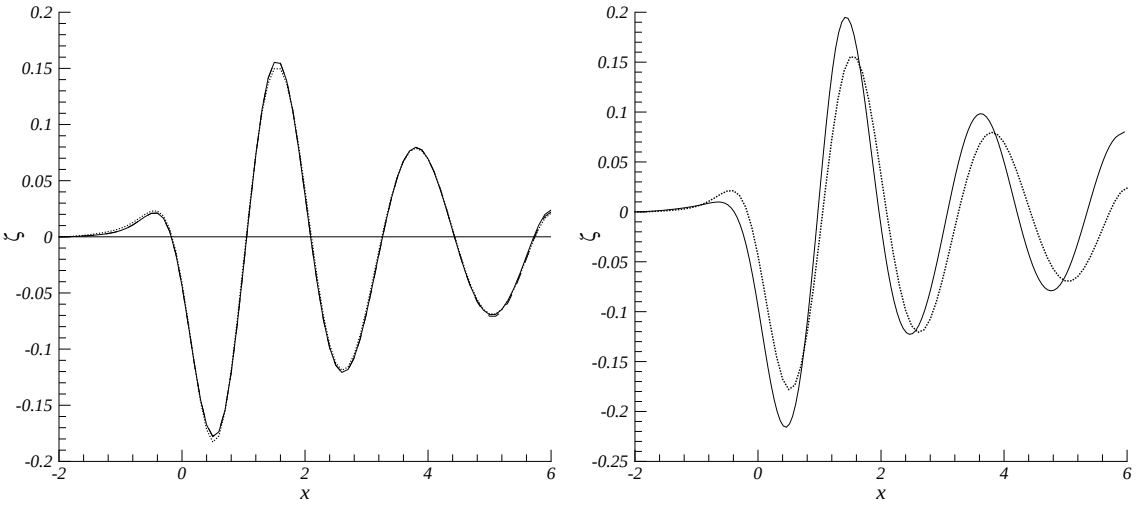

Figure 2: Wave elevations in the plane $y = 0$ for the Gaussian pressure perturbation with $P = 0.05$. *Left:* of the present free-surface Navier-Stokes method on Ω_h; initial ($\zeta = 0$), $n = 1$ (dotted), $n = 2$ (dashed), and $n = 3$ (solid). *Right:* of the potential-flow method from [3] (solid) and the present Navier-Stokes method (dotted).

In Figure 2, $\zeta = \eta/\eta_{max}$ is the wave elevation divided by the maximum obtainable elevation $\eta_{max} = \frac{\mathrm{Fr}^2}{2}$. The last iterate in the left graph of Figure 2 shows a wave length of $\lambda = 2.3$ and a maximum scaled amplitude of about 15%. These results correspond fairly well with the results obtained through the potential-flow method described in [4]. For further comparison purposes a solution for this test case has also been computed through the potential-flow method described in [3]. The corresponding wave pattern is shown in the right graph of Figure 2, together with the present Navier-Stokes solution (the dotted line). Differences between both wave patterns are to be attributed to differences in the two continuous models as well as their numerical discretizations. In Figure 3 we still show the entire Navier-Stokes wave pattern as obtained after the third free-surface update.

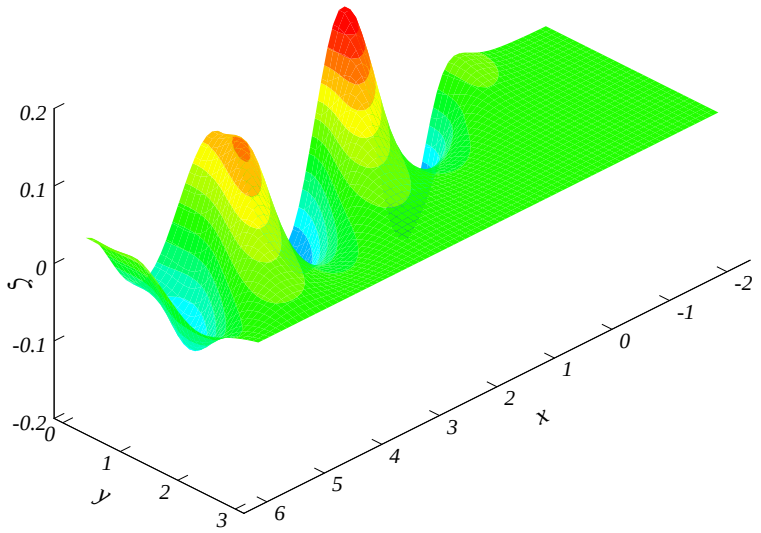

Figure 3: Wave elevation for the Gaussian pressure perturbation with $P = 0.05$, on Ω_h, after three free-surface updates.

4.2 Influence of the outflow boundary condition

The starting divergence of the inner iteration on the third mesh, as shown in Figure 1, is due to an incompatibility between the free-surface flow solution and the underlying bulk-flow boundary condition at the outflow boundary. This discrepancy can be overcome by extending Ω_h with a wave-dissipation zone, see, e.g., [11]. Such a zone is added to rapidly dissipate all the wave energy from the numerical solution, hereby reducing the solution to uniform flow conditions.

The wave energy is better dissipated by increasing the numerical viscosity. This is achieved by (*i*) reducing the accuracy of the discretization of (2.7) in the wave-dissipation zone to first order, and (*ii*) by applying grid stretching in the wave-dissipation zone. The grid-point distribution in the wave-dissipation zone is controlled by

$$x_i = x_{\text{out}} e^{\alpha \frac{\Delta x}{x_{\text{out}}} i}, \quad y_j = y_e e^{\alpha \frac{\Delta y}{y_e} j}, \quad i = 1, \ldots, (N_x)_{\text{add}}, \quad j = 1, \ldots, (N_y)_{\text{add}}, \tag{4.1}$$

where α is the stretching factor in x- and y-direction, and where $(N_x)_{\text{add}}$ and $(N_y)_{\text{add}}$ are the numbers of additional points in both directions. Both numbers are fixed by specifying the maximally allowable mesh width, e.g., $|x_{(N_x)_{\text{add}}} - x_{(N_x)_{\text{add}}-1}|$ is set at 0.5. The same is done for the y-direction. The extended mesh has $149 \times 53 \times 31$ points. In absence of a wave solution near the outflow plane the incompatibility between the free-surface flow and the bulk flow disappears and a homogeneous Neumann condition for the pressure can be specified as outflow boundary condition.

On this extended domain we computed five free-surface updates. The positive influence of the wave-dissipation zone on the convergence behavior of both the inner and outer iteration can be clearly seen when comparing Figure 4 with Figure 1.

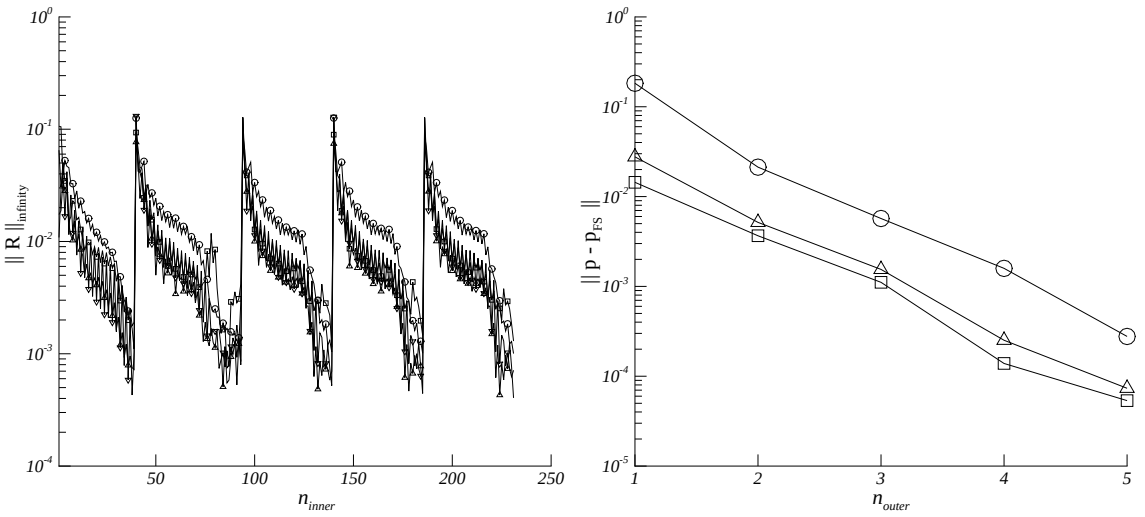

Figure 4: Convergence histories for the Gaussian pressure perturbation with $P = 0.05$, on Ω_h with wave-dissipation zone. *Left:* of the inner-iteration process, $\mathbf{R}$ is the residual of the continuity equation (Δ), the x-momentum equation ($\Box$), the y-momentum equation (∇), and the z-momentum equation ($\bigcirc$), only every fourth marker is shown. *Right:* of the free-surface pressure defect; measured in L_1-norm ($\Box$), L_2-norm (Δ), and L_∞-norm ($\bigcirc$).

In Figure 5, we show the entire wave pattern as obtained after the fifth free-surface update. The wave damping in the dissipation zone, which starts at $x = 10$, is clearly visible.

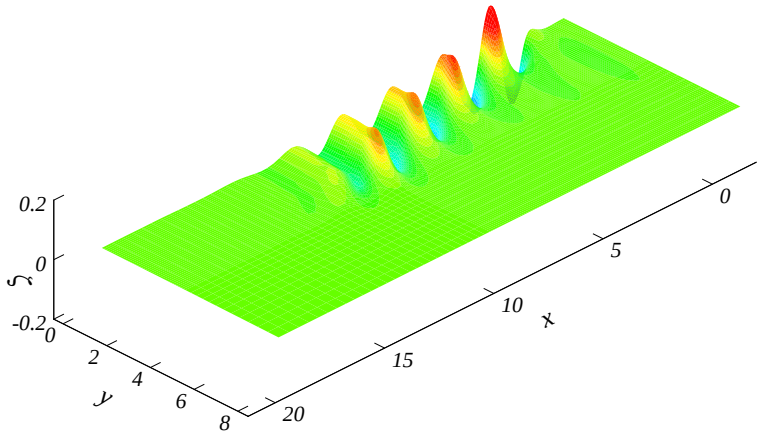

Figure 5: Wave elevation for the Gaussian pressure perturbation with $P = 0.05$, on Ω_h with dissipation zone, after five free-surface updates.

In Figure 6, we still depict the elevations after the first and fifth free-surface update, in the planes $y = 0$ and $y = 2$. Particularly from the left graph in Figure 6, it appears that the free-surface iteration converges very fast. (The initial estimate for the free surface is the line $\zeta = 0$.) Note that, as opposed to the first iterate in the left graph of Figure 6 and as opposed to the three iterates in the left graph of Figure 2, the free surface in the symmetry plane, as obtained after the fifth update, shows a small trough at about $x = -1$. The trough can still be observed at $y = 2$ (the right graph of Figure 6).

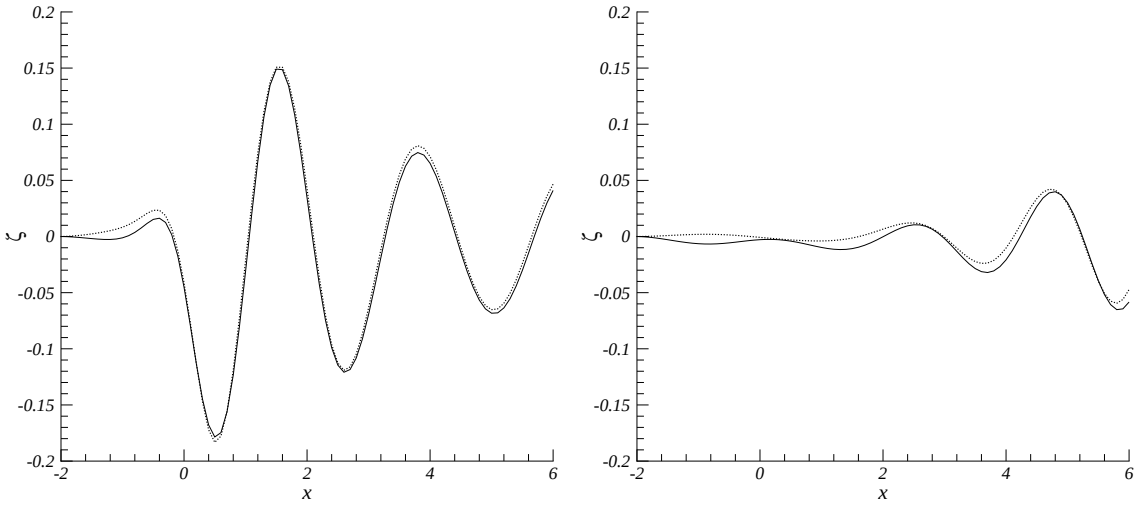

Figure 6: Wave elevation for the Gaussian pressure perturbation with $P = 0.05$, on Ω_h with wave-dissipation zone; $n = 1$ (dotted) and $n = 5$ (solid). *Left:* In the plane $y = 0$. *Right:* In the plane $y = 2$.

In Figure 7 we plotted our Navier-Stokes wave patterns in the symmetry plane, as obtained on the domains *with* and *without* wave-dissipation zone. For comparison purposes, in Figure 7 we also give the wave pattern obtained with the potential-flow method described in [3]. Differences between the two Navier-Stokes wave patterns in Figure 7 may be attributed mainly to the fact that the solution on the domain without wave-dissipation zone is less far converged than that on the domain with wave-dissipation zone. Still concerning Figure 7, note the strong wave damping starting from $x = 10$, the x-coordinate of the upstream boundary of the wave-dissipation zone.

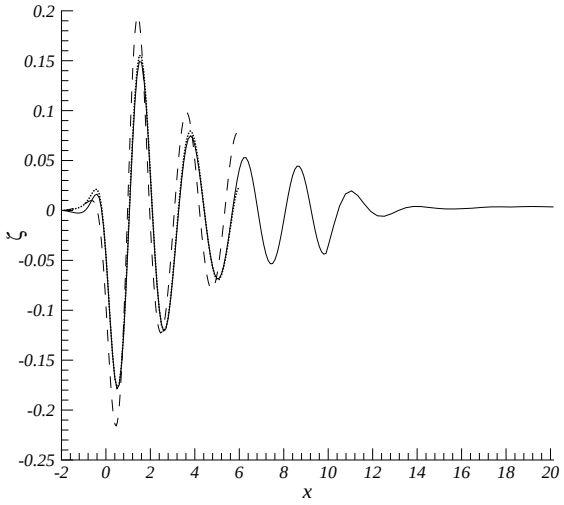

Figure 7: Wave elevation in the plane $y = 0$ for the Gaussian pressure perturbation with $P = 0.05$; present Navier-Stokes method, on Ω_h with and without wave-dissipation zone (solid and dotted, respectively), and potential-flow method from [3] (dashed).

4.3 Mesh-width study

In this section, the effects of the mesh width on the convergence and accuracy of the solution are investigated. This is done by comparing the numerical results obtained for Ω_h with results obtained for Ω_{2h} and $\Omega_{\frac{h}{2}}$. To reduce the influence of the outflow boundary condition a wave-dissipation zone is added to each of the three grids.

Convergence behavior of inner and outer iteration The convergence of the inner iteration on Ω_{2h} and $\Omega_{\frac{h}{2}}$ is shown in Figure 8. It appears that the strategy for the solution of the Navier-Stokes subproblems is not (yet) optimally efficient. To further illustrate this, in Figure 9, we have plotted n_{inner}, the number of inner iterations needed for the first Navier-Stokes subproblem, versus N_x, the number of grid points in x-direction. A least-squares fit reveals a linear dependence of n_{inner} on N_x. (Ideally, n_{inner} is independent of N_x; this may be realized with a proper multigrid method.)

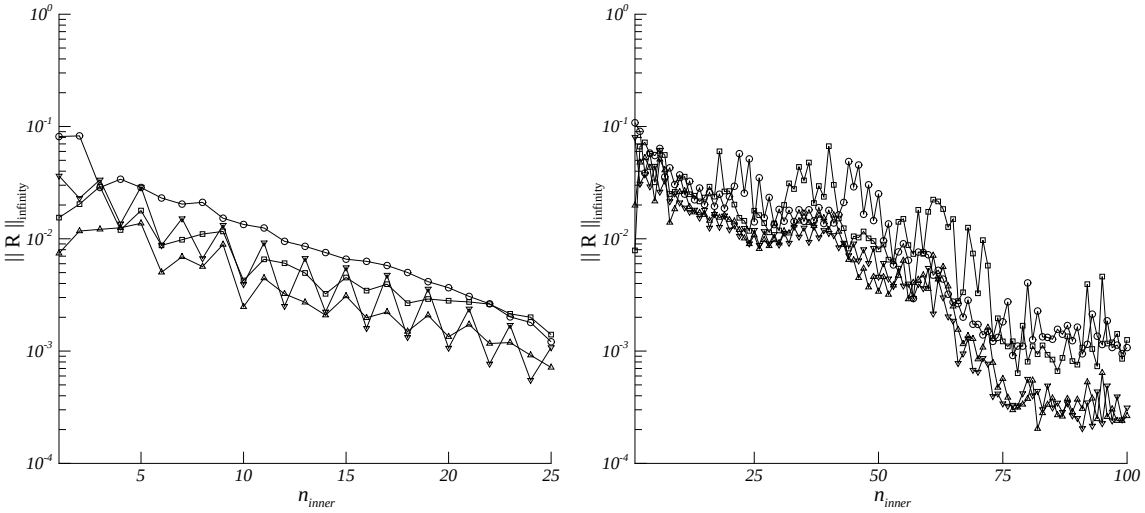

Figure 8: Convergence histories of the inner-iteration process for the Gaussian pressure perturbation with $P = 0.05$, with wave-dissipation zone, $\mathbf{R}$ is the residual of the continuity equation (Δ), the x-momentum equation ($\Box$), the y-momentum equation (∇), and the z-momentum equation ($\bigcirc$), only every fourth marker is shown. *Left:* on Ω_{2h}. *Right:* on $\Omega_{\frac{h}{2}}$.

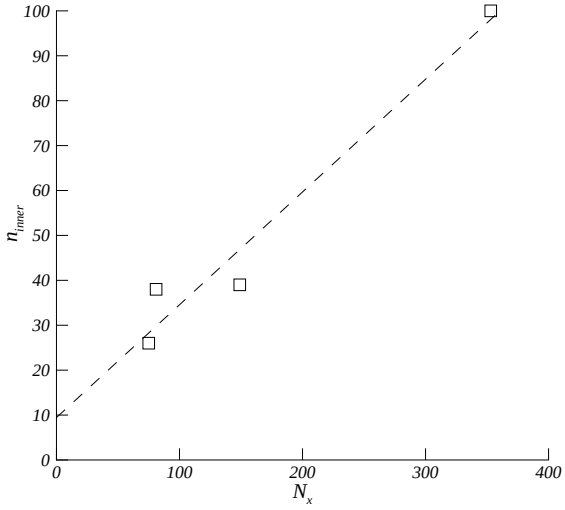

Figure 9: Required number of inner iterations in first Navier-Stokes subproblem versus the number of grid points in x-direction.

The outer iteration's convergence behavior on the three grids (Ω_{2h}, Ω_h, $\Omega_{\frac{h}{2}}$) is shown in Figure 10. Comparing the three convergence rates from $n_{outer} = 2$ to $n_{outer} = 3$, it appears that the convergence is fairly grid-independent.

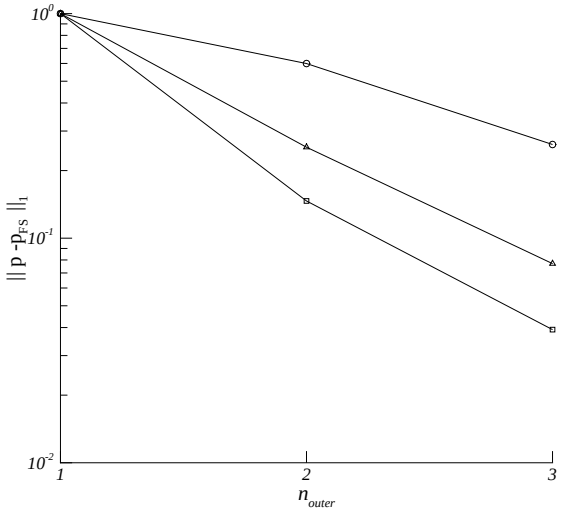

Figure 10: Convergence histories of the outer-iteration process for the Gaussian pressure perturbation with $P = 0.05$, with wave-dissipation zone, measured in L_1-norm; on Ω_{2h} (□), Ω_h (Δ), and $\Omega_{\frac{h}{2}}$ (◯).

Accuracy behavior For the three grids, the wave elevations in the plane $y = 0$ are shown in Figure 11. They show a clear dependence of the wave length and wave amplitude on the mesh width. These effects can be attributed to the discretization of the quasi free-surface boundary condition. In (2.7), $\mathbf{u} \cdot \nabla p$ is discretized using the $\mathcal{O}(h^2)$ upwind scheme. The mesh-width dependence can be understood through a spectral analysis of (2.7). The dominant term in (2.7) is up_x; for first analysis purposes, (2.7) is reduced to $up_x = 0$. For u positive, the corresponding modified equation reads

$$u\frac{\partial p}{\partial x} = u\frac{h^2}{3}\frac{\partial^3 p}{\partial x^3} - u\frac{h^3}{4}\frac{\partial^4 p}{\partial x^4} + \mathcal{O}(h^4). \tag{4.2}$$

Inserting a single wave solution of the form $p = Pe^{\mathrm{i}kx}$, the spectral representation of the leading term results in

$$uik\left(1 + \frac{1}{3}h^2k^2\right)Pe^{\mathrm{i}kx} = \mathcal{O}(h^3). \tag{4.3}$$

From this relation it can be concluded that the numerical advection velocity of p increases with increasing mesh width, thus increasing the length of the gravity wave. The latter increase can be explained from the dispersion relation for waves on deep water, see [10]. Particularly when applying a multigrid solution strategy, one should be aware of the mesh dependency of the wave lengths.

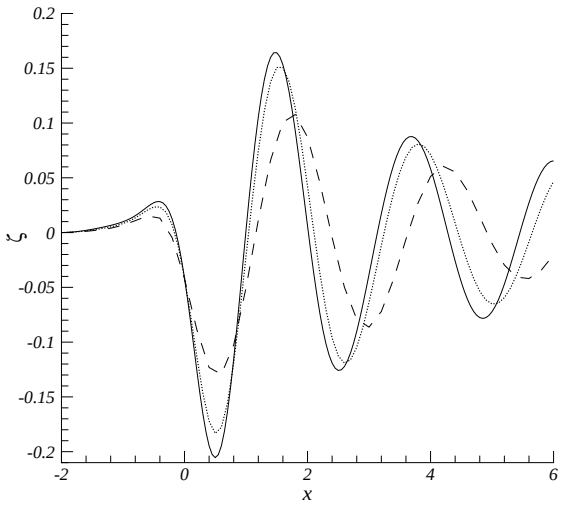

Figure 11: Wave elevation in the plane $y = 0$ for the Gaussian pressure perturbation with $P = 0.05$; on Ω_{2h} (dashed), Ω_h (dotted), and $\Omega_{\frac{h}{2}}$ (solid), all with wave-dissipation zone.

4.4 Higher-order discretization of quasi free-surface boundary condition

As a next step, we replace the $\mathcal{O}(h^2)$ upwind discretization of $\nabla\varphi$ in (3.11) by an $\mathcal{O}(h^3)$ upwind scheme. Then, the modified equation reads

$$u\frac{\partial p}{\partial x} = -u\frac{h^3}{12}\frac{\partial^4 p}{\partial x^4} + \mathcal{O}(h^4), \tag{4.4}$$

showing no dispersion error, but a fourth-order dissipation error, which is responsible for a decrease of the wave elevation. Note that the fourth-order dissipation error is smaller than that of (4.2). A comparison of the solution obtained with the two schemes, after a single free-surface update, is shown in Figure 12, together with the results obtained through the potential-flow method described in [3]. As expected, the $\mathcal{O}(h^3)$ scheme gives slightly higher waves. But it also yields a slightly less fast convergence of both the inner and outer iteration than the $\mathcal{O}(h^2)$ scheme (compare Figure 13 and Figure 4). In the remainder of this paper we do not use the $\mathcal{O}(h^3)$ discretization of the quasi free-surface boundary condition.

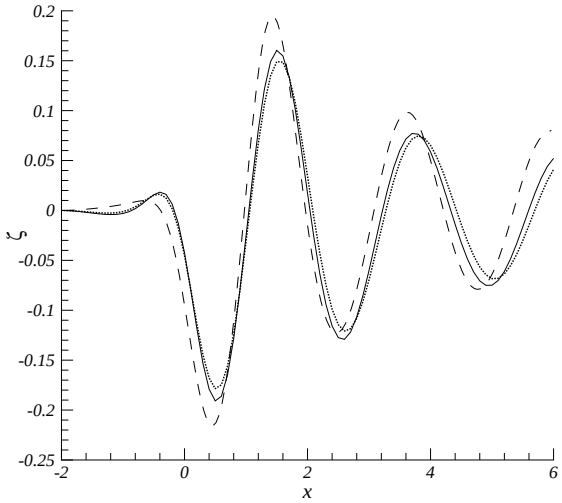

Figure 12: Wave elevation in the plane $y = 0$ for the Gaussian pressure perturbation with $P = 0.05$; for the Navier-Stokes method on Ω_h with wave-dissipation zone, $\mathcal{O}(h^3)$ scheme (solid) and $\mathcal{O}(h^2)$ scheme (dotted); and for the potential-flow method from [3] (dashed).

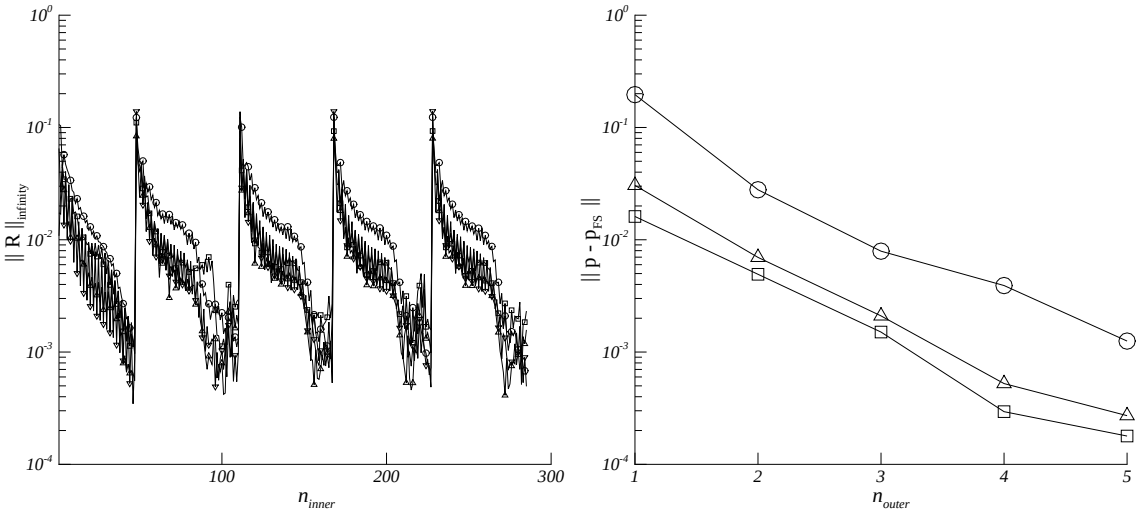

Figure 13: Convergence histories for the Gaussian pressure perturbation with $P = 0.05$, on Ω_h with wave-dissipation zone, with $\mathcal{O}(h^3)$ discretization of the quasi free-surface boundary condition. *Left:* of the inner-iteration process, $\mathbf{R}$ is the residual of the continuity equation (Δ), the x-momentum equation ($\square$), the y-momentum equation (∇), and the z-momentum equation ($\bigcirc$), only every fourth marker is shown. *Right:* of the free-surface pressure defect; measured in L_1-norm ($\square$), L_2-norm (Δ), and L_∞-norm ($\bigcirc$).

4.5 Case with increased amplitude

The present numerical study concerns the computation of the wave pattern on Ω_h, for a stronger imposed pressure perturbation. The amplitude of the perturbation is increased from $P = 0.05$ to $P = 0.2$, leaving the other parameters unaltered. The convergence history of the inner iteration is shown in the left graph of Figure 14. The computed wave elevation, in the plane of symmetry, is shown in the right graph of Figure 14. This figure shows that the deepest trough has fallen off to approximately $\zeta = -0.88$, instead of $\zeta = -0.18$ for the $P = 0.05$ case, which indicates that the wave system behaves nonlinearly.

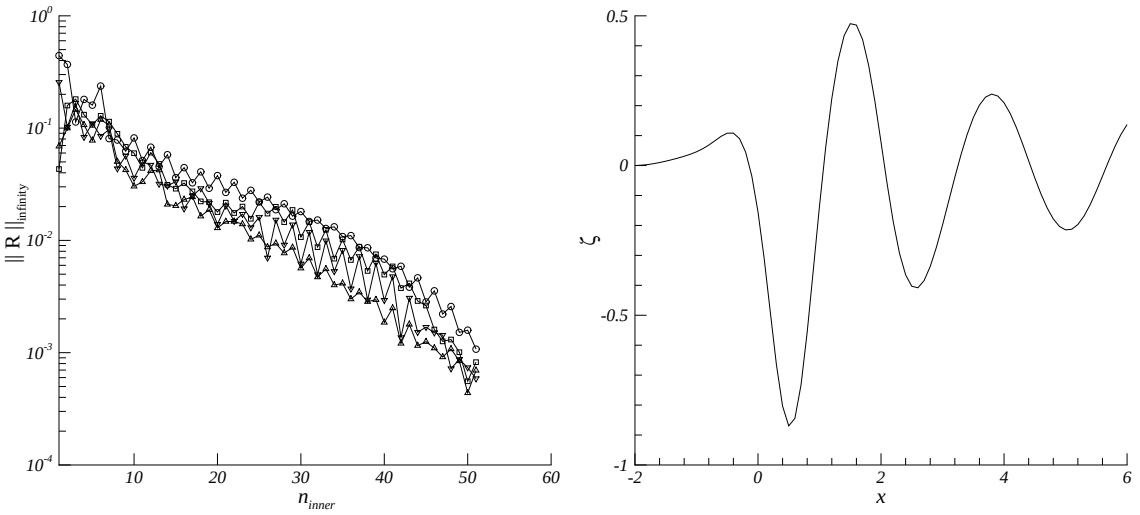

Figure 14: Computational results for the Gaussian pressure perturbation with $P = 0.2$, on Ω_h with wave-dissipation zone. *Left:* convergence history of the inner-iteration process, $\mathbf{R}$ is the residual of the continuity equation (Δ), the x-momentum equation ($\Box$), the y-momentum equation (∇), and the z-momentum equation ($\bigcirc$), only every fourth marker is shown. *Right:* wave elevation in the plane $y = 0$.

4.6 Case with flat plate

We proceed by investigating the performance of our free-surface Navier-Stokes method in the presence of a viscous boundary layer which intersects the free surface. The water-height formula (3.1) has no difficulty when coinciding with a no-slip boundary condition. Free-surface displacement formulae based on the velocity defect normal to the free surface may have so. They may need a modification at and near no-slip boundaries. What may need attention though in our free-surface algorithm is the quasi free-surface boundary condition, (2.7). When it coincides with a no-slip boundary, and when $p_{\mathrm{FS}} = 0$ (or close to zero), in that neighborhood, (2.7) boils down to $\lim_{\mathbf{u}\downarrow 0} \mathbf{u} \cdot \nabla p = 0$, which implies ill-posedness of ∇p (and hence p) in that region.

We perform numerical experiments for the case with a flat plate at $y = 0$, $-1 \leq x \leq 3$, $\forall z$, with $\mathrm{Re} = 10^6$, and with the pressure perturbation still imposed to the free surface and according to (3.10), with $P = 0.05$, $\alpha = -4$ and $(x_c, y_c) = (0, 0)$. The results reveal that our method still converges, be it slower than in the case without flat plate (compare Figure 15 with Figure 4).

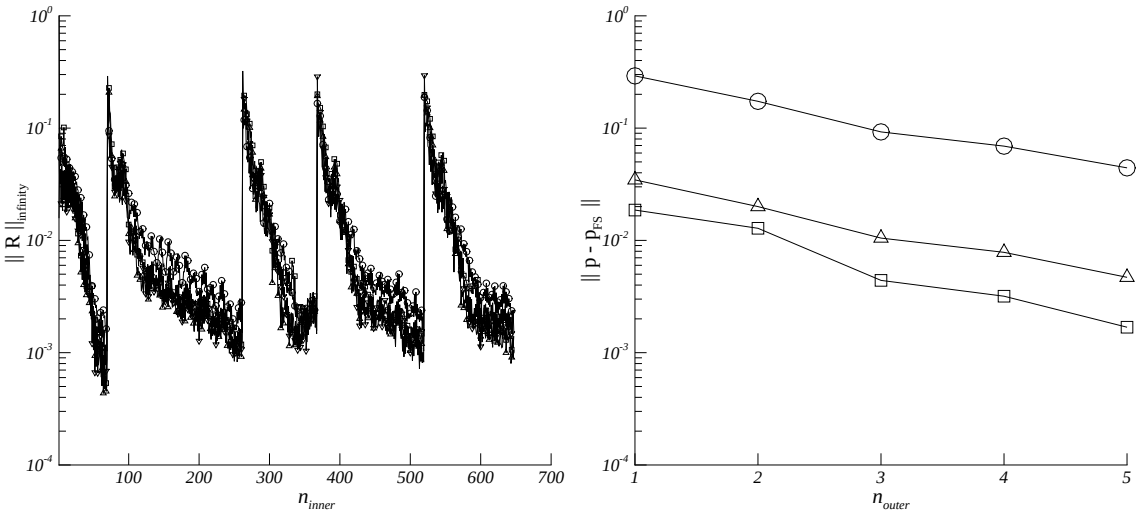

Figure 15: Convergence histories for flat plate combined with Gaussian pressure perturbation with $P = 0.05$, on Ω_h with wave-dissipation zone. *Left:* of the inner-iteration process, $\mathbf{R}$ is the residual of the continuity equation (Δ), the x-momentum equation ($\square$), the y-momentum equation (∇), and the z-momentum equation ($\bigcirc$), only every fourth marker is shown. *Right:* of the free-surface pressure defect; measured in L_1-norm ($\square$), L_2-norm (Δ), and L_∞-norm ($\bigcirc$).

The flat plate seems to have a remarkably strong influence on the wave pattern (Figure 16). If this is the case indeed, already for this test case there would be a strong motivation for the *simultaneous computation* of wave phenomena and viscous phenomena (through a free-surface Navier-Stokes method), instead of the *classical split computation* of both types of phenomena (through, e.g., a free-surface potential-flow method and a flat-surface Navier-Stokes method). We assume that the significant difference between both wave patterns is to be explained mainly by the still coarse resolution of the boundary layer, which is expected to cause a large discretization error.

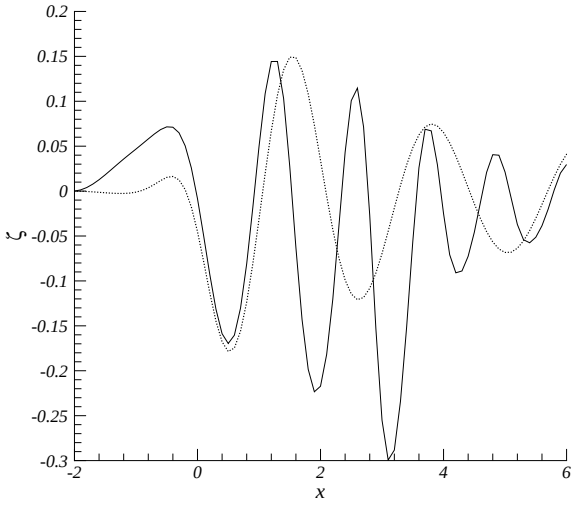

Figure 16: Wave elevation in the plane $y = 0$, on Ω_h with wave-dissipation zone; with flat plate (solid) and without flat plate (dotted).

5. Modified algorithm and numerical results

5.1 The modified algorithm

The free surface algorithm as described in Section 3.1 is computationally efficient but the efficiency may be further improved. Alternatingly, the existing algorithm (i) completely solves the Navier-Stokes equations with the free surface frozen, and (ii) updates the free surface with the Navier-Stokes flow

frozen. Complete solution of the Navier-Stokes flow per free-surface update may be unnecessary. Here we investigate the alternative approach of updating the free surface after each relaxation sweep in the Navier-Stokes solver. The modified algorithm still alternates between the bulk-flow update and the free-surface update (the complexity of a monolithic solution of Navier-Stokes flow and free surface is still avoided), but the frequency of alternating is much higher than in the original algorithm. Summarizing, the modified free-surface algorithm reads:

I. For a given boundary Γ_{FS}, perform a relaxation sweep to

$$\begin{aligned} &\mathcal{C}(\mathbf{u}(\mathbf{x}),\varphi(\mathbf{x}))=0, \quad \forall \mathbf{x}\in\Omega,\\ &\mathcal{B}(\mathbf{u}(\mathbf{x}),\varphi(\mathbf{x}))=0, \quad \forall \mathbf{x}\in\Gamma_0, \end{aligned}$$

$$\left.\begin{aligned} &\mathbf{t}^{(\alpha)}\cdot\tau(\mathbf{u})\cdot\mathbf{n}=0, \quad \alpha=1,2\\ &\mathrm{Fr}^2\mathbf{u}\cdot\nabla\varphi-\mathbf{u}\cdot\mathbf{e}_z=\mathrm{Fr}^2\mathbf{u}\cdot\nabla p_{\mathrm{FS}} \end{aligned}\right\}, \quad \forall \mathbf{x}\in\Gamma_{\mathrm{FS}}.$$

II. Use the new iterate $(\mathbf{u}(\mathbf{x}),\varphi(\mathbf{x}))^T$ of I to obtain a new approximation of Γ_{FS} according to

$$\{(x,y,z:=\mathrm{Fr}^2(\varphi(\mathbf{x})-p_{\mathrm{FS}}(\mathbf{x})) : \forall \mathbf{x}\in\Gamma_{\mathrm{FS}}\},$$

If $\parallel R \parallel_\infty < \epsilon_{\mathrm{NS}}$ and if $\parallel p-p_{\mathrm{FS}} \parallel_\infty < \epsilon_{\mathrm{FS}}$ then stop, else goto I.

5.2 First results

The modified algorithm described in the previous section is now applied to compute the gravity waves for the $P=0.05$ case without flat plate, leaving the other parameters unaltered as well. The computation is performed on the grid Ω_h with the same dissipation zone as before. As a measure of convergence we will still monitor the residuals of the governing Navier-Stokes equations and the pressure defect at the free surface (Figure 17).

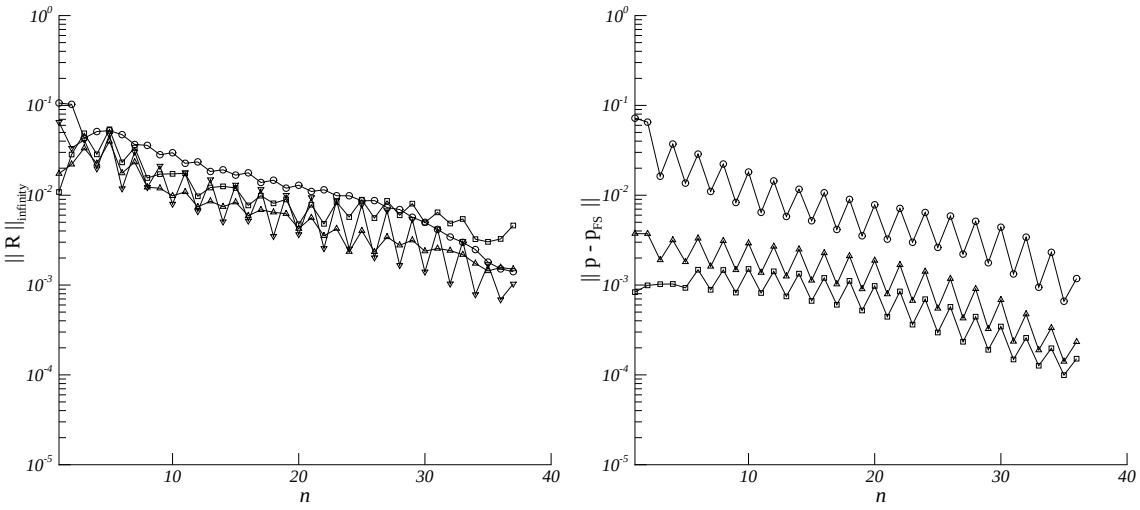

Figure 17: Convergence histories for the Gaussian pressure perturbation with $P=0.05$, computed with the modified algorithm, on Ω_h with wave-dissipation zone. *Left:* of the inner iteration process, $\mathbf{R}$ is the residual of the continuity equation (Δ), the x-momentum equation ($\square$), the y-momentum equation (∇), and the z-momentum equation ($\bigcirc$). *Right:* of the free-surface pressure defect; measured in L_1-norm ($\square$), L_2-norm (Δ), and L_∞-norm ($\bigcirc$).

Remarkable in Figure 17 is the very regular oscillation in the convergence history of the free-surface residual $\parallel p-p_{\mathrm{FS}} \parallel$. This oscillatory behavior is explained by the fact that the Navier-Stokes solver alternates between symmetric and one-sided (downwind) relaxation sweeps, an experimentally found optimal relaxation strategy from which we do not deviate. Comparing the total amounts of computational work put into the original algorithm and the modified algorithm (the left graphs in Figures 4 and 17, respectively), it appears that the modified algorithm is about six times more efficient than the

original, a significant improvement. The convergence history of the wave elevation in the symmetry plane is depicted in Figure 18.

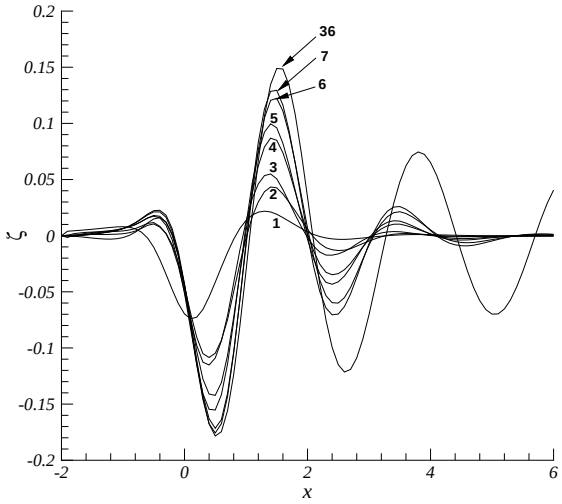

Figure 18: Convergence history of the wave elevation in the plane $y = 0$ for the Gaussian pressure perturbation with $P = 0.05$, computed with the modified algorithm, on Ω_h with wave-dissipation zone, numbers denote the iteration counter.

As expected, in comparison to the original algorithm, the modified algorithm needs more free-surface updates, but the computational work between two consecutive free-surface updates is of course very much less. Figure 18 nicely shows how the wave train literally unfolds itself; the first iterate (marked in Figure 18) shows a significant (though still far from converged) trough, a still very modest wave crest downstream and practically no waves still further downstream. In the following iterates, besides increasingly larger wave amplitudes, also an increasingly longer wave train arises. A consequence of this more evolutionary convergence of the free surface is that the Navier-Stokes method starts each relaxation on a grid that is less different from the preceding grid as compared to the original algorithm. As a consequence, *besides more efficient*, the modified algorithm is *also more robust*. The greater robustness manifests itself in, e.g., the fact that higher wave elevations can be obtained (to be shown in the next section).

5.3 Further results

To give an impression of the good robustness of the modified algorithm, in Figures 19–24 we present free-surface results for computations with successively $P = 0.2, 0.3$ and 0.4. The larger P, the more iterations are required, but the algorithm remains to be convergent. In the $P = 0.4$-case, a relative water height of more than 80% is obtained (Figure 24).

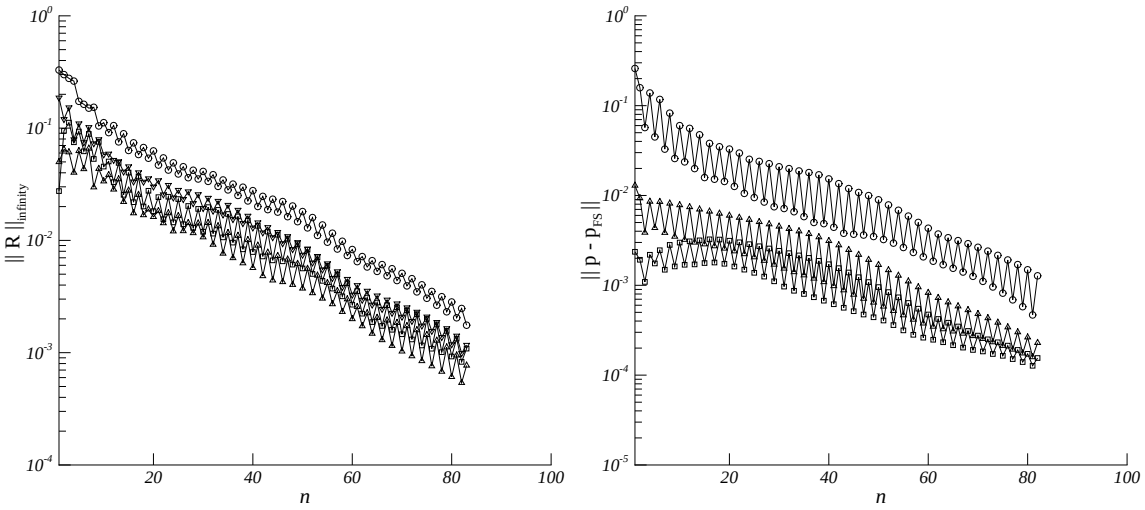

Figure 19: Convergence histories for the Gaussian pressure perturbation with $P = 0.2$, computed with the modified algorithm, on Ω_h with wave-dissipation zone. *Left:* of the inner-iteration process, $\mathbf{R}$ is the residual of the continuity equation (Δ), the x-momentum equation ($\square$), the y-momentum equation (∇), and the z-momentum equation ($\bigcirc$). *Right:* of the free-surface pressure defect; measured in L_1-norm ($\square$), L_2-norm (Δ), and L_∞-norm ($\bigcirc$).

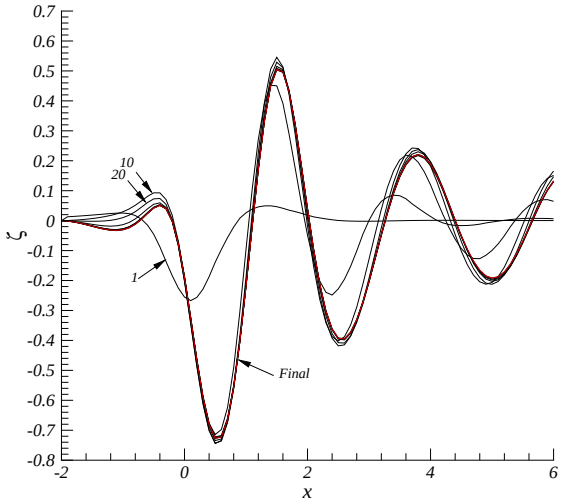

Figure 20: Convergence history of the wave elevation in the plane $y = 0$ for the Gaussian pressure perturbation with $P = 0.2$, computed with the modified algorithm, on Ω_h with wave-dissipation zone, numbers denote the iteration counter, final iteration number is 82.

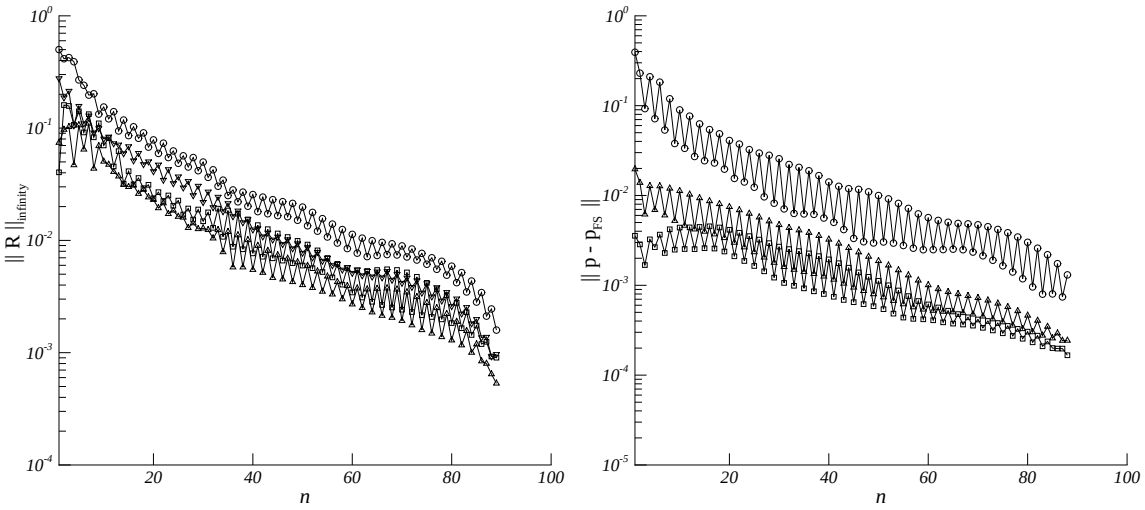

Figure 21: Convergence histories for the Gaussian pressure perturbation with $P = 0.3$, computed with the modified algorithm, on Ω_h with wave-dissipation zone. *Left:* of the inner-iteration process, $\mathbf{R}$ is the residual of the continuity equation (Δ), the x-momentum equation ($\square$), the y-momentum equation (∇), and the z-momentum equation ($\bigcirc$). *Right:* of the free-surface pressure defect; measured in L_1-norm ($\square$), L_2-norm (Δ), and L_∞-norm ($\bigcirc$).

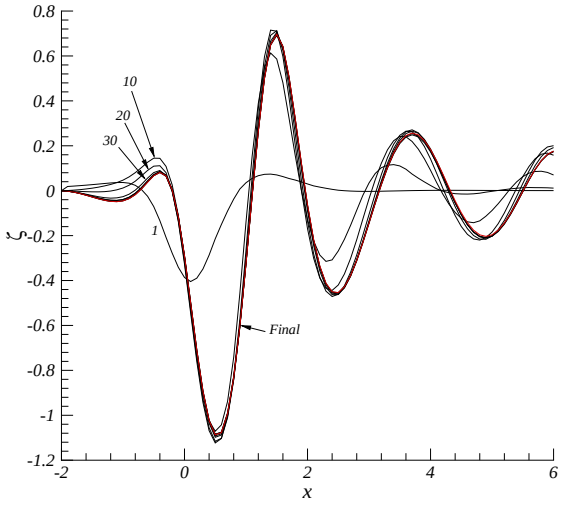

Figure 22: Convergence history of the wave elevation in the plane $y = 0$ for the Gaussian pressure perturbation with $P = 0.3$, computed with the modified algorithm, on Ω_h with wave-dissipation zone, numbers denote the iteration counter, final iteration number is 88.

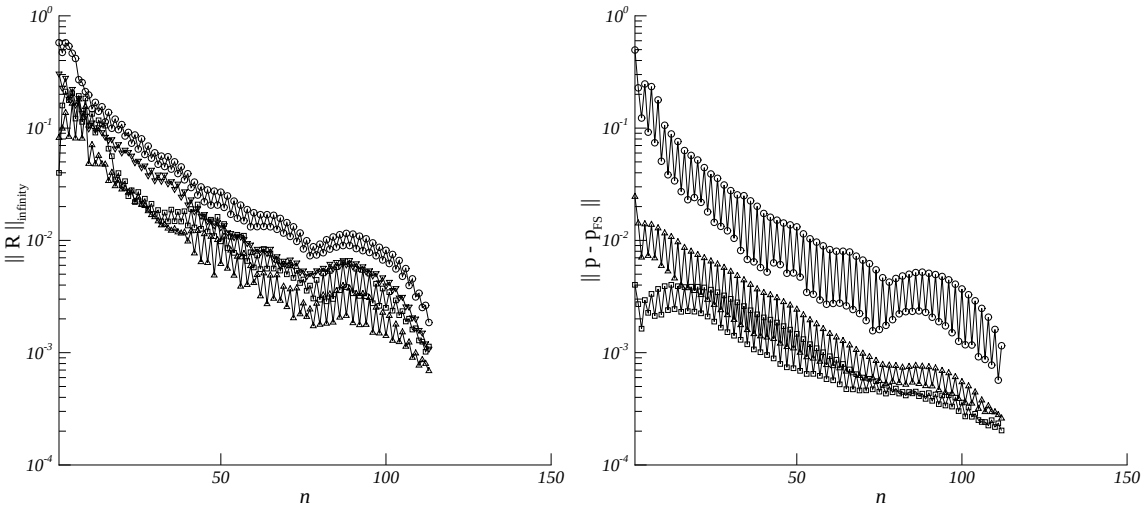

Figure 23: Convergence histories for the Gaussian pressure perturbation with $P = 0.4$, computed with the modified algorithm, on Ω_h with wave-dissipation zone. *Left:* of the inner-iteration process, $\mathbf{R}$ is the residual of the continuity equation (Δ), the x-momentum equation ($\Box$), the y-momentum equation (∇), and the z-momentum equation ($\bigcirc$). *Right:* of the free-surface pressure defect; measured in L_1-norm ($\Box$), L_2-norm (Δ), and L_∞-norm ($\bigcirc$).

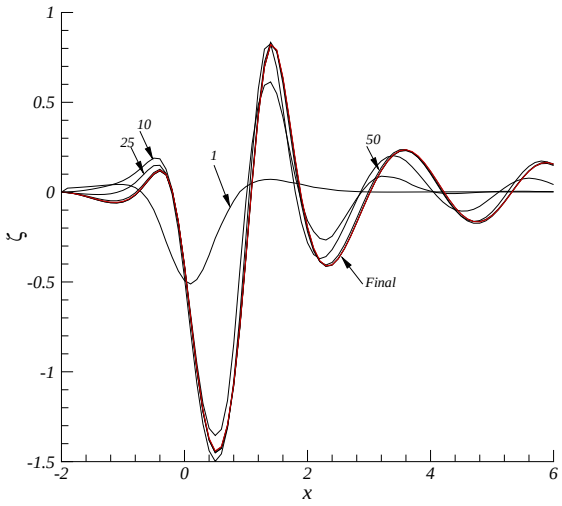

Figure 24: Convergence history of the wave elevation in the plane $y = 0$ for the Gaussian pressure perturbation with $P = 0.4$, computed with the modified algorithm, on Ω_h with wave-dissipation zone, numbers denote the iteration counter, final iteration number is 113.

6. Conclusions

Solution of the steady, free-surface Navier-Stokes equations through a time-stepping approach is known to be inefficient, particularly in 3D. Recently, for the 2D, free-surface Navier-Stokes equations, Van Brummelen et al. have proposed a non-monolithic free-surface algorithm that does not follow a time-stepping approach. In the present paper we have extended this algorithm to 3D and have applied it to flow problems simulating the flights over open water of hovercraft at different weights.

Our results show that, for convergence purposes, it makes sense (i) to take the computational domain sufficiently large and (ii) to discretize the quasi free-surface boundary condition only first-order accurate in the far field. (In this way, unperturbed far-field boundary conditions can be imposed.)

The considered 3D free-surface algorithm appears to quickly yield the proper 3D wave physics. The free-surface pressure defect appears to converge almost grid-independently. For linear and mildly nonlinear wave systems, free-surface iteration may not even be necessary though; only a single free-surface update may be sufficient for finding the wave pattern to within engineering accuracy.

Numerical computations for a case in which a no-slip boundary intersects the free surface (crucial for ship hydrodynamics) show that the method maintains its good convergence properties. In case the boundary layer is not accurately resolved, the no-slip boundary condition has a strong influence on the wave pattern.

An important result of the paper is the proposed reduction of the inner iteration to a single work unit only (a single relaxation sweep). This reduction yields a significant improvement in both efficiency and robustness. This modified version of the free-surface algorithm is expected to be useful to ship hydrodynamics in an industrial context.

References

1. Koren B, Lewis MR, van Brummelen EH, van Leer B. Riemann-problem and level-set approaches for two-fluid flow computations, I. Linearized Godunov scheme. *Report MAS-R0112*, CWI: Amsterdam, 2001.
2. van Brummelen EH, Raven HC, Koren B. Efficient numerical solution of steady free-surface Navier-Stokes flow. *Journal of Computational Physics* 2001; **174**: 120–137.
3. Raven HC. A solution method for the nonlinear ship wave resistance problem. *PhD thesis*, Delft University of Technology: Delft, 1996.
4. Wyatt DC. Development and assessment of a nonlinear wave prediction methodology for surface vessels. *Journal of Ship Research* 2000; **44**: 96–107.
5. Alessandrini B, Delhommeau G. Simulation of three-dimensional unsteady viscous free surface flow around a ship model. *International Journal for Numerical Methods in Fluids* 1994; **19**: 321–342.
6. Campana E, Di Mascio A, Esposito PG, Lalli F. Viscous-inviscid coupling in free surface ship flows. *International Journal for Numerical Methods in Fluids* 1995; **21**: 699–722.
7. Farmer J, Martinelli L, Jameson A. A fast multigrid method for the nonlinear ship wave problem with a free surface. In *Proceedings of the Sixth International Conference on Numerical Ship Hydrodynamics*, Patel W, Stern F (eds); National Academy Press: Washington D.C., 1994; pp. 155–172.
8. Tzabiras GD. A numerical investigation of 2D, steady free surface flows. *International Journal for Numerical Methods in Fluids* 1997; **25**: 567–598.
9. Hoekstra M. Numerical simulation of ship stern flows with a space-marching Navier-Stokes method. *PhD thesis*, Delft University of Technology: Delft, 1999.
10. Lighthill MJ. *Waves in Fluids*. Cambridge University Press: Cambridge, 1958.
11. Israeli M, Orszag S. Approximation of radiation boundary conditions. *Journal of Computational Physics* 1981; **41**: 115–135.

Table of Contents